

pubs.acs.org/cm Article

High Ionic Conductivity and Cost-Effective Halide Solid Electrolyte Enabled by Long-Range Cooperative Transport in Bi-Doped Li₂ZrCl₆

Ruishan Zhang, Shunning Li, Feng Pan, and Bingkai Zhang*



Cite This: Chem. Mater. 2025, 37, 8261-8271



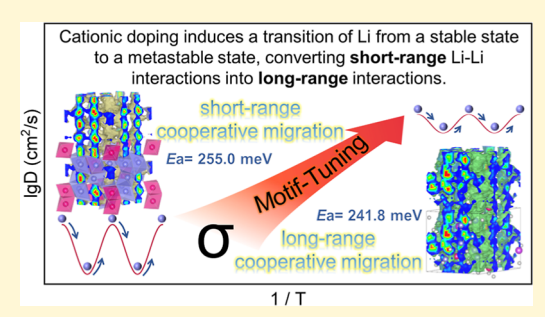
ACCESS

III Metrics & More

Article Recommendations

Supporting Information

ABSTRACT: Li₂ZrCl₆ (LZC), a halide-based solid-state electrolyte, combines high ionic conductivity with cost-effectiveness, yet its atomic-scale ion transport mechanisms and doping strategies are insufficiently understood. Using first-principles calculations and ab initio molecular dynamics (AIMD) simulations, we first evaluated the intrinsic Li-ion migration behavior in bulk LZC. Potential energy surface analysis based on Li-ion site energies, combined with AIMD calculations, confirms the potential promotional effect of bismuth (Bi) cation doping on bulk ionic conductivity, increasing it to 10.93 mS cm⁻¹ and reducing the activation energy to 241.77 meV. Experimental results also demonstrate that Bi doping significantly enhances the electrical conductivity of LZC. This improvement is attributed to a transition from short- to long-range cooperative



Li-ion migration. Additionally, 50% bromine (Br) substitution helped to reduce energy fluctuations caused by cation disorder, leading to a more uniform migration pathway. Statistical analysis across multiple solid-state electrolyte (SSE) systems further showed that shorter nearest-neighbor Li–Li distances are strongly correlated with higher conductivity and lower activation energies. This work highlights the importance of local structure and short-range interactions in halide SSEs and proposes a Bi-doped LZC as a cost-effective, high-performance candidate for next-generation solid-state batteries.

1. INTRODUCTION

All-solid-state batteries (ASSBs) have emerged as a pivotal direction for next-generation energy storage technologies, attracting significant attention from both academia and industry due to their high energy density, enhanced safety, and long cycle life. 1,2 However, the commercialization of ASSBs still faces several challenges, including the low intrinsic conductivity of solid-state electrolytes (SSEs), high interfacial resistance between electrodes and electrolytes, and underdeveloped large-scale manufacturing techniques. As the core component of ASSBs, SSEs are required to possess high conductivity,^{4,5} excellent (electro)chemical stability,^{6–8} and economic viability, underscoring the importance of developing such materials.⁶ Among various candidates, halide SSE has attracted growing interest due to its favorable properties. In particular, Li₂ZrCl₆ (LZC) has emerged as a promising halide SSE⁹⁻¹¹ owing to its use of an abundant and inexpensive 10 central metal element, scalable synthesis routes, and high electrochemical performance in ASSBs. 12

Cation doping has proven effective in further improving the conductivity and electrochemical properties of LZC-based SSE. Recently, Tu et al. synthesized LZC with a room-temperature conductivity of 4.46×10^{-4} S cm⁻¹, which meets the requirements for rapid ion transport in SSEs. ¹³ Zhang et al. demonstrated that doping 25% Al³⁺ into Li_{2.25}Zr_{0.75}Al_{0.25}Cl₆ increased the oxidation potential from 4.10 to 4.30 V. ¹⁴ Xie et al. improved the room-temperature conductivity to 1.19×10^{-3} S cm⁻¹ by Y doping (Li_{2.5}Zr_{0.5}Y_{0.5}Cl₆), ¹⁵ while Jung et al.

synthesized LZC with a room-temperature conductivity of 4.0 \times 10⁻⁴ S cm⁻¹, which meets the requirements for rapid ion transport in SSEs, and maintained a conductivity of 1.0×10^{-3} S cm⁻¹ with Fe doping.¹¹ In/Sc-doped Li_{2-x}Zr_{1-x}M_xCl₆ even achieved a peak conductivity of $2.1 \times 10^{-3} \text{ S cm}^{-1}$ (x = 0.70). Nazar et al. further optimized the $Li_{3-x}Zr_{1-x}M_xCl_6$ (M = Y and Er) system, achieving a conductivity of 1.4×10^{-3} S cm⁻¹ at 25 °C, ¹⁷ highlighting the critical role of cation doping. In addition, Ganesan et al. proposed a progressive fluorination strategy for synthesizing $\text{Li}_2\text{ZrCl}_{6-x}\text{F}_x$ (0 $\leq x \leq$ 1.2), which significantly enhances its interfacial stability against Li metal anodes. 18 These studies demonstrate that the chemical composition of LZC can be effectively tailored through both anion and cation doping, thereby optimizing its electrochemical performance and interfacial compatibility. However, to date, there have been few systematic studies on the effects of different cation dopants on the electrochemical performance of LZC, particularly regarding the underlying Li-ion transport mechanisms and their tunability within the LZC framework. The local structural motifs and short-range interactions in

Received: July 2, 2025 Revised: October 9, 2025 Accepted: October 10, 2025 Published: October 15, 2025





LZC-based materials play critical roles in governing the electrochemical behavior of SSEs, particularly their ionic conductivity.

In this work, we conducted a comprehensive computational investigation of Li-ion transport mechanisms and material design strategies in crystalline LZC and its doped derivatives. To modulate the ionic transport behavior and gain deeper insights into the structure-property relationship, a series of cation-doped compounds with the general formula $Li_{2+x}Zr_{1-x}M_xCl_6$ (LZMC, M = Mg, Mn, Zn, Al, Bi, Cr, Er, Fe, In, Sc, Y, Yb, Hf, Mo, Si, Ti, and Nb) were systematically examined. In particular, bismuth (Bi) and bromine (Br) were selected as representative cationic and anionic dopants, respectively, to elucidate their effects on Li-ion migration pathways and energy barriers. Our results provide mechanistic insights and design principles for developing high-performance chloride-based solid-state electrolytes. First, we employed firstprinciples calculations and ab initio molecular dynamics (AIMD) simulations to characterize the intrinsic ionic transport behavior of pure LZC, including directional migration tendencies and Li-Li correlation effects. To understand how atomic-scale structure influences transport, we constructed the migration energy landscape based on the site energies of octahedral and tetrahedral Li positions and used this framework to evaluate the impact of 17 different cation dopants at the Zr site. These dopants were also assessed in terms of their effects on the thermodynamic, moisture, and electrochemical stability of the LZC system, including the electrochemical window and interfacial compatibility with typical cathodes and sulfide/oxide-based electrolytes. We then selected representative doped systems for in-depth AIMD simulations to investigate their Li-ion transport properties, correlation functions, and structural dynamics. Furthermore, to assess the role of anion chemistry, we explored 50% Brsubstitution in the halide sublattice and analyzed its influence on cation disorder and migration landscape uniformity using 20 different cation-disordered configurations. Finally, we performed a statistical analysis of various SSE systems to examine how nearest-neighbor Li-Li distances correlate with activation energies and ionic conductivities, aiming to identify structural features that favor cooperative transport. This work provides a comprehensive framework for understanding the structure-transport relationships in halide SSEs and offers valuable guidance for the future discovery and design of lowcost, high-performance halide-based materials.

2. METHODOLOGY AND CALCULATION DETAILS

2.1. DFT Methods. All the DFT calculations were implemented in the Vienna Ab Initio Simulation Package with the projector-augmented method. The electron wave function of valence electrons was expanded using the projected augmented wave base set. We employed the generalized gradient approximation level of DFT + D3²² with the Perdew-Burke-Ernzerhof (PBE) exchange-correlation functional to describe the exchange-correlation effects in this study. The plane wave truncation energy of 520 eV and the system's total energy of less than 10^{-5} eV was utilized for all the calculations. The Gamma k-point sampling method was carried out for all calculations with 4 × 4 × 6 k-point samplings. The conductivity was computed using AIMD. Molecular dynamics simulations were performed under the NVT^{24} ensemble to investigate the structural evolution of the material at temperatures ranging from 700 to 1500 K (700,

800, 900, 1000, 1100, 1200, and 1500 K). The Brillouin zone was sampled at the Gamma point, and a plane-wave energy cutoff of 400 eV was adopted (verified to ensure convergence of the energy and forces). A time step of 1 fs was used to resolve the rapid atomic motions at high temperatures. These settings enabled a systematic analysis of temperature-dependent structural dynamics, offering insights into the material's phase transition mechanisms under thermal excitation. Additional computational details can be found in the Electronic Supporting Information.

The formation energy (E_f) is calculated from the binary precursor, and E_f is calculated using eq 1:

$$E_{\rm f} = \frac{E_{\rm LZMC} - (2+4x-xy) \cdot E_{\rm LiCl} - (1-x) \cdot E_{\rm ZrCl_4} - (x) \cdot E_{\rm MCl_y}}{n_{\rm atom}} \end{math}$$

 $E_{\rm LZMC}$ is the energy obtained after structural optimization, and $E_{\rm LiCl}$, $E_{\rm ZrCl_4}$, and $E_{\rm MCl}$, correspond to the energy of the most stable compounds obtained in the Materials Project. x is the doping concentration of M, y is the valence state of M, and n is the atomic number of LZMC.

The Li-ion diffusion behavior in LZC was studied by analyzing AIMD trajectories using self Van Hove correlation functions $(G_s(r,t))$ and distinct Van Hove correlation functions $(G_d(r,t))$, $f(G_d(r,t))$ and $f(G_s(r,t))$ defined as eqs 2 and 3 represents the probability that the same atom moves to $f(G_s(r,t))$ in time t to $f(G_s(r,t))$. Conversely, $f(G_s(r,t))$ then denotes the probability that an atom initially located at position $f(G_s(r,t))$ will be replaced by another atom at $f(G_s(r,t))$ in time $f(G_s(r,t))$ mainly probes the motion of the atoms themselves, while $f(G_s(r,t))$ probes the correlated motion between atoms.

$$G_{s}(t, r) = 4\pi r^{2} \frac{1}{N} \langle \sum_{i=1}^{N} \delta(r - (|r_{i(t)} - r_{i(0)}|)) \rangle$$
 (2)

$$G_{\rm d}(t, r) = 4\pi r^2 \frac{1}{N} \langle \sum_{i=1}^{N} \sum_{j=1}^{N} \delta(r - (|r_{i(t)} - r_{j(0)}|)) \rangle$$
 (3)

To quantitatively characterize Li-ion diffusion, we computed the mean-square displacement $(MSD)^{27}$ from AIMD trajectories using the DiffusionAnalyzer²⁸ module in pymatgen. The MSD is defined as eq 4

$$MSD(t) = \frac{1}{N} \langle |r_{i(t)} - r_{i(0)}|^2 \rangle$$
(4)

where $r_{i(t)}$ denotes the position of the *i*-th Li-ion at time t, and N is the total number of Li-ion. The diffusion coefficient D was derived from the linear regime of the MSD-t curve via the Einstein relation eq 5. All simulations were performed in the NVT ensemble (1000 K, 2 fs time step) to ensure statistical reliability.

$$D(t) = \frac{\text{MSD}(t)}{6t} \tag{5}$$

The site distance functions (SDFs) provide a quantitative description of the real-time displacement behavior of Li atoms relative to their initial positions during the temporal evolution. This function precisely characterizes the trajectory of individual atoms by calculating the geometric distance between the atomic position $r_{(t)}$ at arbitrary time t and the initial position $r_{(0)}$, as shown in eq 6. Through comparative analysis of SDFs curves for different atoms within the same unit cell,

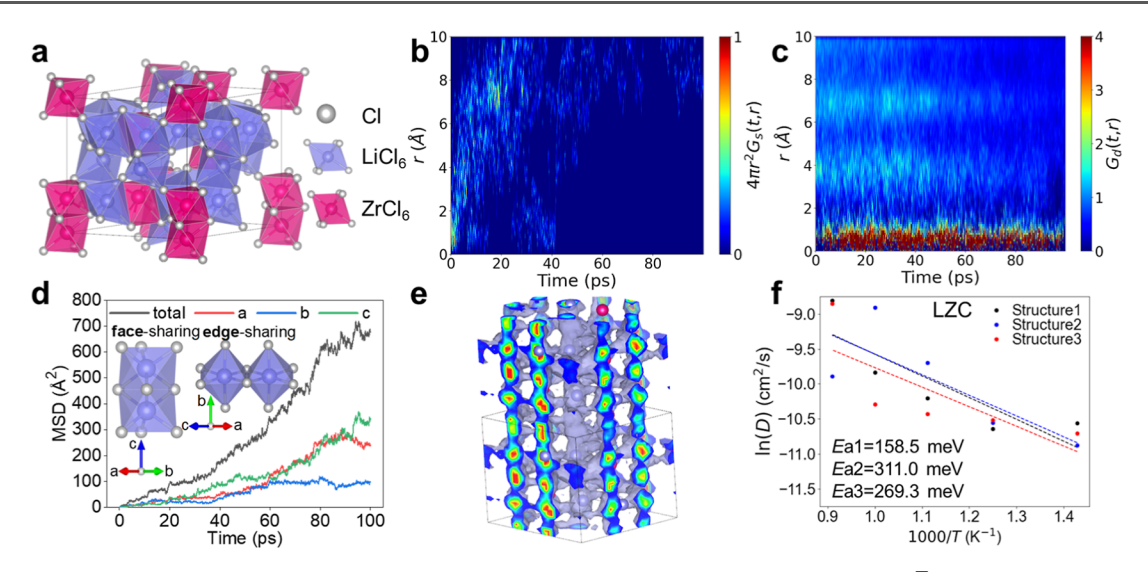


Figure 1. Ionic conductivity and migration mechanism of pure LZC. (a) Crystal structure of LZC with the P3m1 space group. (b–e) All are the data obtained by AIMD simulating the LZC model at a temperature of 1000 K. (b) $G_s(r,t)$ for Li-ion. (c) $G_d(r,t)$ for Li-ion. (d) The MSD of Li-ion in LZC, including Li–Li sharing type of LZC. (e) The trajectory density of Li-ion in LZC. The isosurface level is 0.001 Å⁻³. (f) Temperature-dependent Li-ion conductivity in three differently symmetric LZC structures: Arrhenius plots derived from AIMD simulations performed at 700, 800, 900, 1000, and 1100 K.

this approach enables identification of correlated trajectory patterns, thereby revealing potential cooperative transport mechanisms between specific atomic pairs.

$$SDF(t) = |r_{(t)} - r_{(0)}| \tag{6}$$

2.2. Models. The LZC structure adopted in this study crystallizes in the trigonal system (space group P3m1), as illustrated in Figure 1a. Cation doping (e.g., Al and Y) was applied to substitute Zr sites as shown in Figure S1a of the Supporting Information, and Figure S1b outlines the computational workflow. In LZC with cation disorder, stable Li-Zr configurations were identified by calculating the Madelung potential. Based on these optimized structures, dopant placements were subsequently determined. In the LZC crystal structure (space group P3m1), both Li and Zr atoms are coordinated octahedrally. Specifically, Li atoms occupy the 6g and 6h Wyckoff positions, while Zr atoms are located at the 1a, 1b, and 2d sites. The Cl atoms reside at the 6i position. 18 Importantly, neither Li nor Zr atoms occupy the tetrahedral coordination sites in this structure. The high symmetry of the octahedral units creates additional interstitial space that facilitates ion migration while minimizing lattice distortion and defect formation, thereby enhancing conductivity and transport efficiency.²⁹ The tetrahedral voids exist between adjacent octahedra, offering an additional channel for Li-ion migration. Meanwhile, the Li-Zr framework adopts both corner- and edge-sharing motifs, forming a robust cationic skeleton that imposes minimal constraints on Li-ion mobility. A $1 \times 1 \times 2$ supercell expansion was performed on the pure LZC structure, yielding a model containing 54 atoms. Subsequently, the Zr sites were systematically substituted with 17 cations (Mg, Mn, Zn, Al, Bi, Cr, Er, Fe, In, Sc, Y, Yb, Hf, Mo, Si, Ti, and Nb), all of which have been experimentally reported to enhance the performance of halide SSEs. 11,14-16,30-38 For each dopant, six different substitution concentrations (x = 0.167, 0.333, 0.5, 0.667, 0.833, and 1) were considered. To avoid the fractional occupancies in structures, the Supercell tool³⁹ was employed to generate all

symmetry-inequivalent doped configurations. The Madelung potential was subsequently calculated for hundreds of candidate structures to identify electrostatically favorable doping configurations, which were then adopted as the basis for subsequent computational models. The calculation workflow was managed by the high-throughput computational platform for the solid-state battery materials. 12,40,41

2.3. Experimental Method. To prepare the $\text{Li}_{2+x}\text{Zr}_{1-x}\text{Bi}_x\text{Cl}_6 \ (0 \le x \le 0.5)$ electrolytes, LiCl (Aladdin, ≥99%), ZrCl₄ (Aladdin, ≥99.9%), and BiCl₃ (Aladdin, 99.99%) were mixed in stoichiometric proportions with a total mass of approximately 2 g. The precursors were thoroughly ground and mixed in an agate mortar and then transferred into a ZrO₂ jar (80 mL) containing ZrO₂ balls with diameters of 10 mm and 5 mm, maintaining a ball-to-powder mass ratio of 45:2. The mixture was subsequently milled at 500 rpm for 33 h to obtain the final products. Powder X-ray diffraction (PXRD) data were collected on a Malvern PANalytical Empyrean diffractometer using Cu K α radiation $(\lambda 1 = 1.5406 \text{ Å}, \lambda 2 = 1.5444 \text{ Å}, \text{ and } I2/I1 = 0.5) \text{ in Bragg}$ Brentano geometry. Measurements were performed over a 2θ range of $10-90^{\circ}$ at a scan rate of 0.028° s⁻¹. To prevent decomposition caused by atmospheric humidity, each sample was sealed with a polyimide film, which provided effective protection without affecting the quality of the PXRD data. Electrochemical impedance spectroscopy (EIS) was conducted at 300 K over a frequency range of $1-7 \times 10^{-6}$ Hz with a voltage amplitude of 10 mV using a Biologic SP-300 electrochemical workstation. Powder samples (100g) of Li_{2+x}Zr_{1-x}Bi_xCl₆ were cold-pressed into pellets under a pressure of 3 tons in a poly(ether-ether-ketone) mold with an inner diameter of 10 mm. The pellets were then placed between two stainless steel rods (φ 10 mm), which served as blocking electrodes for the EIS measurements.

3. RESULTS AND DISCUSSION

3.1. Cooperative Li-lon Transport in LZC for SSE Design. To elucidate the intrinsic Li-ion transport mechanism in LZC, we conducted AIMD simulations at elevated

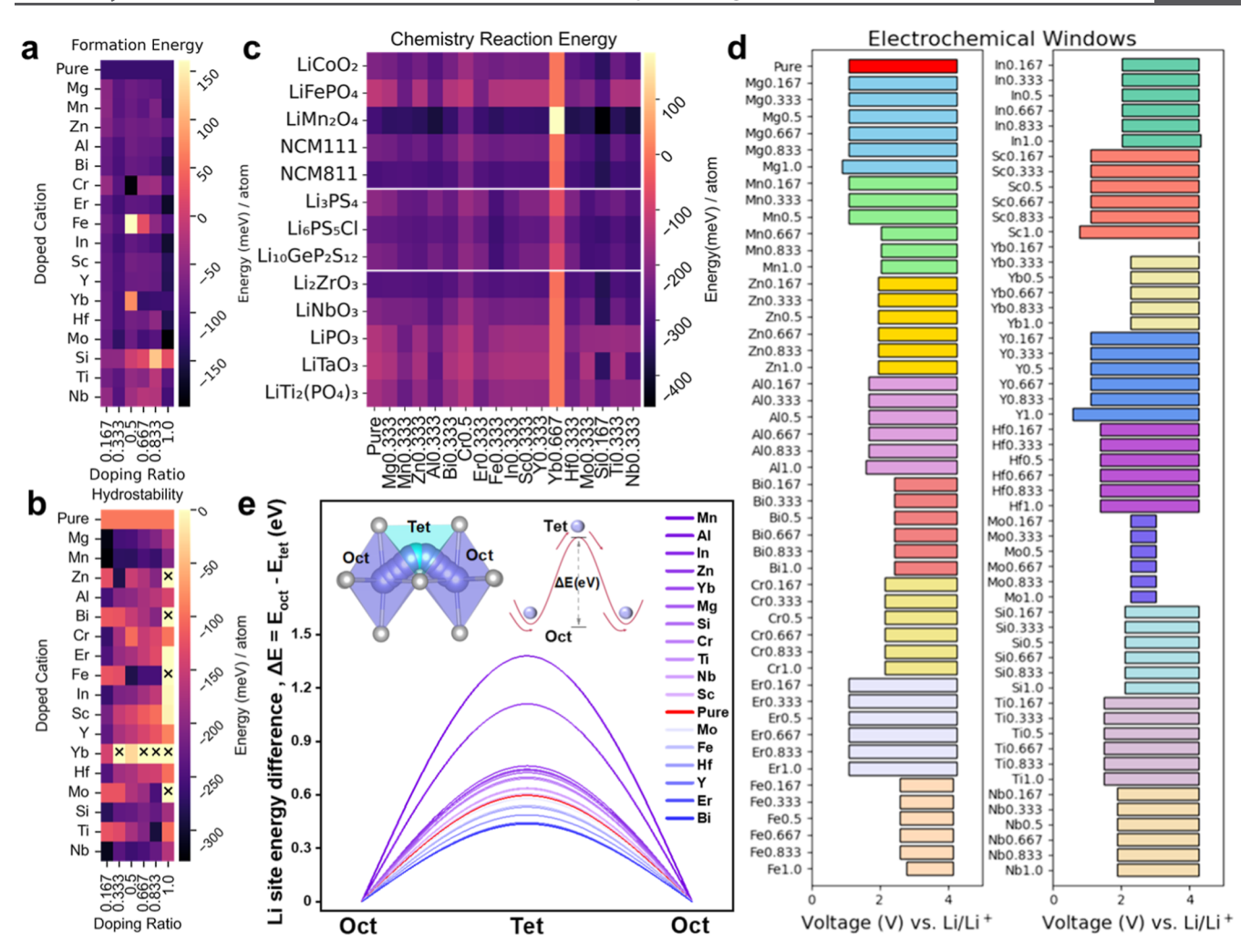


Figure 2. Electrochemical performance comparison of LZMC materials. (a–d) Phase stability and (electro)chemical stability of the LZMC structures. (a) Thermodynamic stability based on formation energy; (b) moisture stability; (c) chemical reaction energy between LZMC and various materials; and (d) electrochemical stability window (ESW) versus Li/Li⁺. (e) Schematic of energy landscape as two different Li sites with different site energy differences.

temperatures of 100 ps. 41 The statistical analysis of Li diffusion was performed by calculating the Li-Li space-time correlation functions, as shown in Figure 1b,c. In Figure 1b, the $G_s(r,t)$ probability density shows one a bright region appearing between 0 and 2.0 Å during the initial $\sim 2-3$ ps, indicating that Li ions primarily undergo vibrations around their equilibrium positions. After 10 ps, the $G_s(r,t)$ probability density exhibits a significantly weakened bright zone, indicating a lower probability of finding a Li-ion around its original position and reflecting the high Li-ion mobility in LZC. In Figure 1c, $G_d(r,t)$ describes the time-dependent probability of finding a Li-ion j at a distance r from a reference ion i, which was located at the origin at t = 0. Throughout the simulation period, a pronounced red band appears at short distances (r <2 Å), indicating that Li-Li interactions predominantly occur near their equilibrium octahedral sites. This short-range Li-Li interaction is indicative of cooperative migration behavior. Similarly, distinct bands are observed at $r = \sim 4$ and ~ 6 Å, indicating significant Li-Li interactions at these distances. Further SDF trajectory analysis of all Li-ions in LZC (Figure S2) reveals that adjacent Li-ions exhibited similar trajectory profiles, supporting the presence of Li-ions cooperative migration. In Figure 1d,e, the MSD results and the trajectory

density of Li-ions (isosurface value = 0.001 Å⁻³) clearly demonstrate that Li-ion conduction in LZC is anisotropic, with dominant migration occurring along the c-axis, facilitated by channels formed through a framework of corner-sharing ZrCl₆ octahedra. The inset in Figure 1d, together with Figure 1a, reveals that in LZC, the LiCl₆ octahedra are connected exclusively via face-sharing along the c-axis, whereas only linear edge-sharing occurs within the ab-plane. The face-sharing arrangement along the c-axis creates a low-energy pathway, rationalizing the enhanced Li-ion mobility in this direction. In contrast, the ab-plane represents the most restricted diffusion pathway, where Li-ion transport proceeds through edgesharing LiCl₆ octahedra interconnected via interstitial tetrahedral sites, indicating that such structural connectivity imposes a higher activation energy (E_a) . Figure 1f presents the calculated Li-ion diffusivity and E_a of LZC, obtained from AIMD simulations across three distinct configurations over the temperature range of 700-1100 K. Supplementary results including MSD, $G_s(r,t)$, and $G_d(r,t)$ of Li-ions dynamics are presented in Figures S3-S5. The calculated ionic conductivities of LZC range from 2.87 to 4.80 mS cm⁻¹, which are slightly higher than experimental values (~0.1-0.446 mS cm $^{-1}$), 10,11,13,15,31,32,42,43 potentially due to factors such as

grain boundary resistance and amorphous domains that are not captured in the idealized crystalline computational models. Based on Arrhenius analysis, $E_{\rm a}$ was determined to lie between 241.60 and 267.96 meV, which falls broadly within the range of reported experimental values ($\sim 260-420$ meV). 10,11,13,18,31,32,42,43

The above findings demonstrate quasi-3D Li-ion transport behavior in the LZC system, where the edge-sharing connectivity of ${\rm LiCl_6}$ octahedra along the b-axis constitutes the rate-limiting structural feature for conductivity. The correlation function analysis confirms the presence of cooperative Li-ion migration mediated by dynamically formed short-range Li–Li interactions. This transport mechanism provides further evidence for its presence in high-ionic-conductivity inorganic solid-state electrolytes. These results highlight the importance of further tuning the Li-ion conductivity through structural and chemical modifications.

3.2. Tuning Phase Stability and Conductivity of LZC via Cationic MCl₆ Units. Assessing the synthetic feasibility of LZMC is essential for rational materials design. To evaluate thermodynamic stability, the formation energies (E_f) of 103 distinct LZMC configurations were calculated, following established methodologies. ⁴⁵ A negative E_f (i.e., more favorable) suggests thermodynamic stability under equilibrium synthesis conditions, whereas a positive E_f implies metastability, potentially hindering experimental realization under standard conditions. Compounds with $E_{\rm f}$ values below 40 meV atom⁻¹ are widely regarded as thermodynamically stable and experimentally accessible. 46,47 In Figure 2a, all calculated formation energies were negative $(E_f < 0)$, confirming the thermodynamic favorability of doped LZC systems. Across all cation-doped configurations, the lowest formation energy consistently occurred at a doping concentration of x = 0.333. Comparative analysis further revealed that with the exception of Fe-, Yb-, and Si-doped systems, all other doped structures exhibited negative $E_{\rm f}$ values, indicative of thermodynamic stability. For instance, the Li_{2.5}Zr_{0.5}Cr_{0.5}Cl₆ system has the lowest E_f ($E_f = -191.19$ meV atom⁻¹), highlighting its exceptional thermodynamic stability. These results collectively affirm the thermodynamic viability of the cation motifengineered LZMC compounds. For moisture stability, 48,49 the reaction energies (ΔE_r) between various LZMC and H₂O are shown in Figure 2b. Compounds marked with an x indicate no chemical reaction with water, suggesting good moisture resistance. Our calculations reveal that pure LZC exhibits limited hydrolytic stability, with a reaction energy of ΔE_r = -93.0 meV atom⁻¹. Notably, Bi, Cr, Sc, Y, and Yb cations exhibit exceptional resistance to moisture-induced degradation, highlighting their potential to enhance the hydrolytic stability of LZC-based electrolytes. A comprehensive evaluation of the interfacial chemical stability of LZMC for ASSB applications considered three key design factors: (1) the necessity of cathode surface coatings, (2) compatibility for use in combination with sulfide electrolytes,⁵⁰ and (3) protective coating needs for LZMC to address air sensitivity. Analysis of the reaction energetics (Figure 2c) demonstrates that nearly all doped systems undergo spontaneous reactions with the cathode materials. For each dopant element, the most thermodynamically stable doping concentration (identified in Figure 2a) was selected for further investigation. Compared to pure LZC, Cr-doped LZC demonstrates the highest interfacial stability among all cation-doped compounds, making it the most promising candidate against the examined cathodes.

LiFePO₄ is identified as the most compatible cathode material, exhibiting the least exothermic reaction energies across all tested LZC-based electrolytes. The study further demonstrates that nearly all cation-doped LZC systems generally can maintain favorable interfacial stability with oxide-based coating materials, outperforming typical sulfide-based solid-state electrolytes in this regard. Our calculations indicate that the reaction between the two predominantly yields binary halides. In practical batteries, such reactions have a negligible impact on performance and therefore are generally not addressed experimentally. In addition, we evaluated the reaction energies between common oxide coating materials and the electrolyte. As shown in Figure 2c, the reaction energies between the chloride electrolyte and oxide coatings are relatively low, suggesting that a coating strategy could be employed to mitigate interfacial reactivity. The reaction energies and detailed reaction pathways between LZC and various compounds, including common cathode materials, sulfide electrolytes, and oxide coatings, are summarized in Table S1 of the Supporting Information.

The ESW was also evaluated through grand potential phase diagram calculations as a function of Li chemical potential,⁵¹ with the results summarized in Figure 2d. For more details on the ESW calculations, please refer to the Calculation Details of ESI. The pure LZC material exhibits an ESW of 3.18 V, with an oxidation limit of 4.27 V and a reduction limit of 1.09 V. Cation doping was observed to significantly influence the ESW, with certain dopants broadening the window while others narrowed it. Notably, Mg_{1.0}, Sc_{1.0}, and Y_{1.0} doping substantially expanded the ESW by decreasing the reduction potential to 0.89, 0.77, and 0.58 V, respectively. In contrast, Fe, Yb, and Mo doping significantly narrowed the ESW. For instance, Yb_{0.167} led to a complete collapse of the ESW, indicating severe electrochemical instability, while Mo doping drastically narrowed the window to 0.75 V (oxidation: 3.01 V and reduction: 2.26 V). Other dopants, including Mn, Zn, Al, Bi, Cr, In, Yb, Hf, Mo, Si, Ti, and Nb, also reduced the ESW to varying degrees. Interestingly, Mn doping only affected the ESW at higher concentrations, whereas low-level In doping (0.167 mol %) had a minimal impact. A comprehensive summary of all ESW-related reactions is provided in Table S2.

It is essential to systematically investigate the influence of cation doping on the conductivity of the LZMC structure. To this end, the migration energy barrier was prioritized, as its exponential dependence in the Arrhenius equation makes it the key factor determining ionic conductivity. As illustrated in the inset of Figure 2e, the Li-ion migration pathway involves alternating occupancy of octahedral (Oct) and tetrahedral (Tet) sites. By calculating the site energy difference between the Oct and Tet positions, we systematically explored how different MCl₆ structural units modulate these site energies within the LZMC framework (Figure 2e). For each LZMC composition, two representative disordered configurations were selected, and statistically meaningful migration barriers were obtained through averaged calculations. As shown in Figure 2e, the site energies of the Tet sites are consistently higher than those of the Oct ones in all cases. Cation doping can significantly tune the energy difference $(\Delta E_{\text{site}})^{52}$ between these two sites. A flatter energy profile, i.e., a smaller ΔE_{site} indicates a reduced energy gap between the Oct and Tet sites, which facilitates cooperative Li-ion migration with lower activation barriers, thereby enhancing conductivity. The results demonstrate that dopants such as Bi, Er, Y, Hf, Fe, and Mo

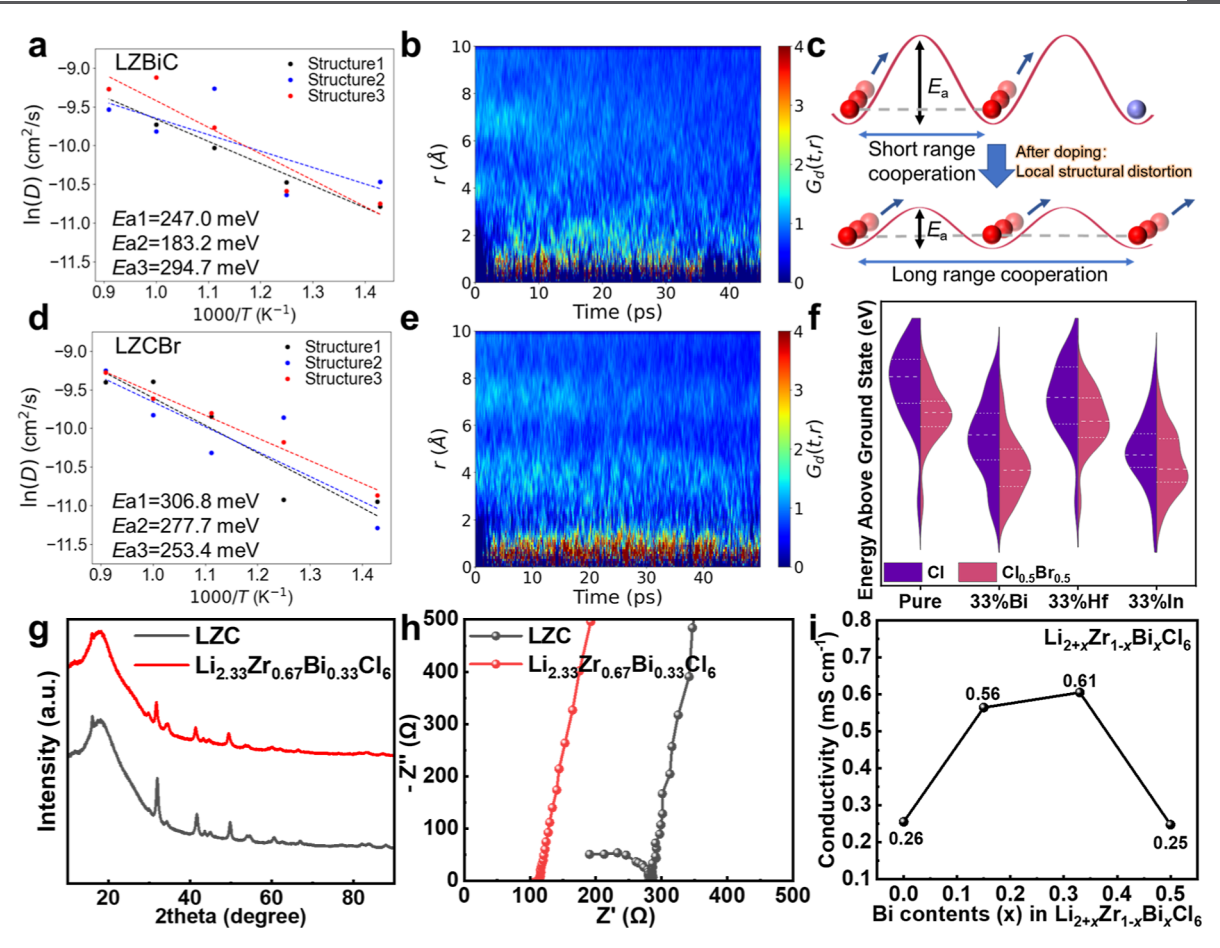


Figure 3. Ionic conductivity and migration mechanism of LZBiC and LZCBr materials. (a,d) Diffusion coefficient (D) at different temperatures of LZBiC and LZCBr, respectively. The corresponding activation energies are given. (b,e) $G_{\rm d}(r,t)$ of the van Hove correlation function for the Li motion in LZBiC and LZCBr, respectively. (c) Schematic illustration of short-range and long-range Li-ion migration. (f) Energy distribution comparison of 20 structures before and after Br-doping for pure LZC, LZBiC, LZHfC, and LZInC. (g) XRD patterns of LZC and $Li_{2.33}Zr_{0.67}Bi_{0.33}Cl_6$. (h) The Nyquist plots of the EIS measurement results of LZC and $Li_{2.33}Zr_{0.67}Bi_{0.33}Cl_6$. with nonreversible electrodes. (i) Ionic conductivities as a function of Bi doping concentration.

effectively reduce $\Delta E_{\rm site}$, promoting higher Li-ion mobility. In contrast, dopants such as Mn, Al, In, Zn, Yb, Mg, Si, Cr, Ti, Nb, and Sc substantially increase the $\Delta E_{\rm site}$, which is detrimental to Li-ion diffusion.

3.3. Enhancing Li-lon Transport in LZC via Bi Cation and Br Anion Doping. For cation doping, the Bi-doped $\text{Li}_2\text{Zr}_{0.667}\text{Bi}_{0.333}\text{Cl}_6$ (LZBiC) system was selected as a representative case for comprehensive AIMD calculations owing to its small site energy difference between Li tetrahedral and octahedral sites. To ensure a fair comparison with pure LZC, the Li stoichiometry in LZBiC was intentionally kept at 2. For LZBiC, the calculated Li-ion diffusivity and E_a are presented in Figure 3a, with the corresponding activation energies summarized in the inset table. The calculated roomtemperature conductivity ranges from 1.62 to 26.53 mS cm⁻¹, with a corresponding E_a between 183.17 and 294.69 meV. Compared to the pristine LZC, doping effectively increases the lower bound of conductivity. Considering that experimentally synthesized crystals often exhibit structural imperfections and lower symmetry than the idealized structures used in theoretical calculations, the predicted lower-limit conductivities may provide more meaningful guidance for experimental design and practical applications. Figure S6 shows the Li-ion trajectories, indicating a 3D migration behavior. Supplementary results of LZBiC including MSD, $G_s(r,t)$, and $G_d(r,t)$ of Li-

ions dynamics are presented in Figures S7-S9. The MSD analysis further reveals that Bi doping significantly enhances Liion mobility along all three crystallographic axis. These results again suggest that Li-ion migration is more favorable along pathways composed of face-sharing octahedra than those formed by edge-sharing octahedra. However, the density plots of $G_d(r,t)$ (Figures 3b and S7–S9) reveal a noticeable decrease in the probability of finding Li-ions within the $r = \sim 0-2$ Å range near the Oct sites at various temperatures, suggesting that short-range Li-Li interactions weaken during Li-ion migration. The high ionic conductivity and low E_a in LZBiC most likely originate from a long-range cooperative Li-ion transport mechanism. To understand the long-range cooperative migration, a simple and intuitive idea is illustrated in Figure 3c. In materials with high E_a , Li-ions tend to vibrate around their equilibrium positions with small displacement amplitudes, leading to strong red intensity in the $r = \sim 0-2$ Å range, as illustrated in Figure 1c. In contrast, in materials with low E_a, Li-ions exhibit larger displacement amplitudes and move further from their equilibrium positions, resulting in weaker red intensity in the same range. These findings highlight a distinct difference in transport behavior between LZBiC and pure LZC, shifting from a localized, short-range cooperative motion to a more delocalized, long-range migration process. It should be noted that the stoichiometric

Li content in LZBiC is 2. In fact, the substitution of Zr^{4+} with Bi^{3+} introduces additional Li-ions into tetrahedral sites, effectively increasing the Li-ion concentration, which in turn further enhances the ionic conductivity. Therefore, further efforts are needed to continue tuning LZBiC in order to achieve an even higher ionic conductivity.

For the Br-anion-doped LZCBr compound, as shown in Figure 3d, the diffusivity versus temperature plots exhibit a room-temperature conductivity ranging from 0.88 to 4.03 mS cm⁻¹ with a corresponding E_a of 253.35–306.83 meV. Supplementary results of LZCBr including MSD, Li-ion trajectories, $G_s(r,t)$, and $G_d(r,t)$ of Li-ions dynamics are presented in Figures S10-S13. Although the conductivity of LZCBr does not show significant improvement compared to pure LZC, the diffusivity data points are notably more concentrated with substantially smaller error bars. This suggests that Br-doping effectively reduces the energy fluctuations arising from cation disorder in the structure. More importantly, similar to LZBiC, the $G_d(r,t)$ of the van Hove correlation function for Li-ion motion, as shown in Figures 3e and S11-S13, again reveals a significantly reduced probability intensity within the short-range region $(r = \sim 0-2)$ Å) between adjacent Li-ions. This observation indicates the occurrence of long-range cooperative migration among the Liions. To understand the impact of Br doping on cationdisordered systems, we evaluated 20 structural configurations via the screening of Madelung potential calculations, including the pure phase and three representative cation-doped systems (Bi, Hf, and In). As shown in Figure 3f, Br doping significantly narrows the energy distribution among different configurations and reduces the variance of their relative energies. This indicates a more uniform potential energy landscape that favors long-range Li-ion transport. This effect is likely attributed to the weaker bonding strength of Li-Br compared to Li-Cl, which softens the M-X-Li-X-M framework and reduces the structure's sensitivity to cation disorder. Therefore, with regard to the role of Br doping, we propose the following explanation: Compared to Cl-, Br- has a larger ionic radius while maintaining the same formal charge. As a result, the charge density on the Br anion is lower, leading to weaker electrostatic interactions with both the framework cations and mobile Li-ions. This reduced interaction results in a more uniform energy landscape. In short, Br doping softens the lattice, thereby facilitating long-range cooperative Li-ion migration. Additionally, we computed the ESW of the Brdoped structure. Compared with LZC, which exhibits a wide window of 1.09-4.27 V, Br doping narrows the stability range to 1.09-3.62 V. Our calculations reveal that Br-substitution in LZC leads to a pronounced lattice expansion: the pristine LZC cell has lattice parameters a = 10.94 Å, b = 11.10 Å, c = 12.05Å, $\gamma = 119.43^{\circ}$, and V = 1274.01 Å³, whereas the Br-containing structure exhibits a = 11.25 Å, b = 11.32 Å, c = 12.48 Å, $\gamma =$ 118.56°, and $V = 1395.27 \text{ Å}^3$. This expansion is consistent with the larger ionic radius of Br⁻ (182 pm) compared to Cl⁻ (167 pm) in 6-fold coordination, as reported by Asano et al. A larger halide anion increases the cation-cation separation, elongates the ionic bonds, and enhances the polarizability of the anion framework, thereby enlarging the accessible migration volume for Li⁺ and reducing steric constraints along conduction pathways. Experimental evidence from Li₃YCl₆ (LYC) and Li₃YBr₆ (LYB) further supports this mechanism: the longer Y-Li distances in LYB (\approx 3.97 Å vs \approx 3.01 Å in LYC) facilitate a three-dimensional network of interconnected migration paths, resulting in a significantly higher room-temperature ionic conductivity (1.7 mS cm⁻¹ for LYB vs 0.51 mS cm⁻¹ for LYC). Importantly, Br-containing halide electrolytes maintain high electrochemical stability against 4 V-class cathode materials without the need for additional surface coatings, indicating that Br-substitution can simultaneously enhance Li-ion transport and preserve interfacial stability. We performed MSD analyses for Cl⁻ and Br⁻ ions in the LZCBr cell (Figure S14), which reveal that Br⁻ exhibits more pronounced mobility than Cl⁻, with a strong dependence on temperature.

To highlight the ionic transport properties of LZBiC and LZCBr, we compared them with several representative SSE materials reported in the literature, as shown in Figure S15. The corresponding E_a and σ for all investigated materials are summarized in Table S3. In halide-based solid electrolytes, interfacial reactions with cathode materials are frequently observed. We systematically analyzed the possible reactions between the three selected electrolytes and representative cathode materials with the detailed results summarized in Table S4. Additionally, Bi is more cost-effective than Zr in its metallic form, and the prices of BiCl₃ and ZrCl₄ are comparable ($\$2.63 \text{ g}^{-1}$ vs $\$3.13 \text{ g}^{-1}$). These results demonstrate that LZBiC and LZCBr exhibit competitive performance as SSE candidates for ASSBs. These considerations suggest that Bi-Br codoping represents a promising strategy to simultaneously enhance structural stability and ionic conductivity in LZC-based electrolytes. Future computational and experimental studies are warranted to systematically explore the synergistic effects of dual doping and optimize the doping concentrations for improved solid-state battery performance.

As shown in Figure 3g, the XRD pattern of LZC exhibits sharp and well-defined diffraction peaks, indicating a high crystallinity. Upon Bi doping, the diffraction peaks shift toward lower angles compared to the pristine phase. This peak shift can be attributed to the larger ionic radius of Bi compared to Zr, confirming the successful incorporation of Bi into the LZC structure. Figure 3h shows the impedance spectra. After Bi doping, the total resistance is significantly reduced, and the Nyquist plot evolves from a large semicircle to a nearly straight line, indicating a much higher ionic conductivity for Li_{2.33}Zr_{0.67}Bi_{0.33}Cl₆ compared to that for LZC. This experimental trend is consistent with the computational predictions. Additionally, we synthesized Li_{2.15}Zr_{0.85}Bi_{0.15}Cl₆ and Li_{2.5}Zr_{0.5}Bi_{0.5}Cl₆ to investigate the influence of the Bi content. As shown in Figure 3i, the ionic conductivity of pristine LZC is 0.26 mS cm⁻¹, while that of $\text{Li}_{2.33}\text{Zr}_{0.67}\text{Bi}_{0.33}\text{Cl}_{6}$ reaches 0.61 mS cm⁻¹. The substantial enhancement in ionic conductivity upon Bi doping confirms its positive effect, although the absolute values are somewhat lower than the calculated values, likely due to the presence of moisture and oxygen during the experimental synthesis, which is inevitable under practical conditions. This observation is consistent with the experimental results reported by Wang et al.⁵⁷

3.4. Correlation between Structural Property and lonic Diffusion in LZC-Based SSEs. As suggested by previous studies, 44,53-55 electrostatic repulsion between adjacent Li ions plays a crucial role in cooperative Li-ion transport. This raises an important question: could the spatial arrangement of nearest-neighbor Li-Li pairs be a key feature governing cooperative ion migration in SSEs. We have previously investigated this systematically, 56 and here we

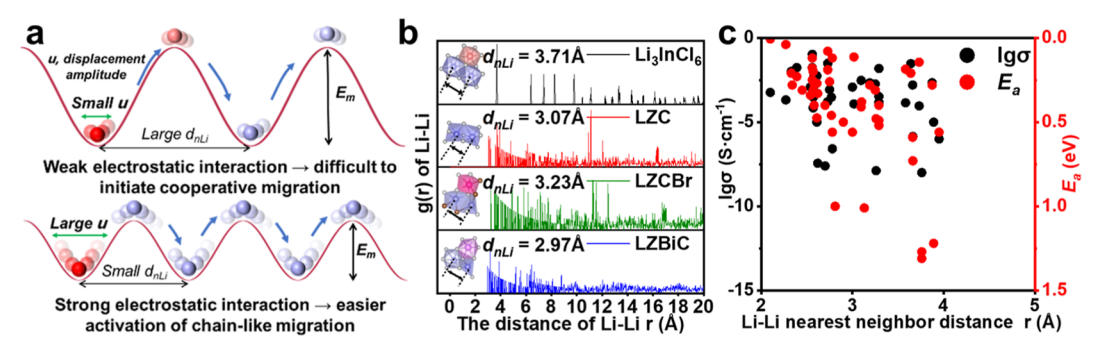


Figure 4. Correlation between nearest-neighbor Li–Li distance and cooperative lithium-ion transport. (a) Schematic of the energy landscape as "activated" by Li-ions (red circle) in SSEs. In materials with small adjacent Li–Li distance, Li-ions vibrate around its equilibrium positions, facilitating more probable activation of chain-like migration. (b) RDF of Li-ions (g(r)) for four LZC-based materials. Li–Li. (c) A correlation between the nearest-neighbor Li–Li distance and both ionic conductivity and E_a was identified based on the literature data.

further examine the correlation between ionic conductivity and $E_{\rm a}$ with the nearest-neighbor Li–Li distances (denoted as $d_{\rm nLi}$) to explore their potential relationship. To explore this, we first proposed a simple and intuitive concept, illustrated in Figure 4a. The figure depicts the energy landscape experienced by Li ions within the lattice framework. In materials with small $d_{\rm nLi}$ Li ions tend to vibrate around their equilibrium positions with a high probability of hopping to adjacent sites, thereby facilitating cooperative migration. In contrast, in materials with larger Li-Li separations, Li ions require larger displacement amplitudes to overcome the migration barrier, which reduces the likelihood of cooperative motion. Guided by this conceptual framework, we analyzed the d_{nLi} by calculating radial distribution functions (RDFs) of Li-ions for Li₃InCl₆, LZC, LZBiC, and LZCBr, all of which exhibit characteristic Li-Li spacings around 3.0 Å, with LZBiC showing the smallest d_{nLi} (Figure 4b). A clear correlation between the d_{nLi} and both ionic conductivity and E_a was identified based on the data compiled from the literature, as illustrated in Figure 4c. Shorter Li-Li distances tend to be associated with higher conductivities and lower E_a , highlighting the critical role of local structural environments in facilitating efficient Li-ion transport. Specifically, materials with d_{nLi} greater than 4 Å rarely achieve the simultaneous optimization of high conductivity and low E_a . In contrast, when d_{nLi} approaches ~3 Å or less, materials tend to exhibit significantly enhanced transport properties, with conductivity exceeding 10^{-4} S cm⁻¹ and E_a falling below 0.30 eV. This correlation between structure and property provides valuable guidance for the rational design and targeted screening of next-generation SSEs. Detailed references and data for Figure 4c are provided in Table S5.

4. CONCLUSION

This study systematically investigates the Li-ion transport mechanisms and design strategies for LZC-based solid-state electrolytes through extensive first-principles calculations. The DFT calculated average room-temperature ionic conductivity and $E_{\rm a}$ of LZC are 3.92 mS cm⁻¹ and 254.83 meV, respectively, which are comparable to the reported experimental values. Importantly, LZC exhibits short-range Li–Li cooperative migration behavior based on the Li-ion correlation functions. Moreover, Li-ion transport along the c-axis is more favorable than in the ab-plane, attributed to the distinct connectivity of LiCl₆ octahedra, face-sharing along the c-axis versus edgesharing in the ab-plane. Based on the energy landscape defined by the site energies of octahedral and tetrahedral Li positions,

the effects of 17 different cation dopants on the migration barrier were systematically evaluated by analyzing the energy differences between these two sites. The results demonstrate that cation doping can significantly reshape the Li-ion E_a profile, thereby effectively tuning the ionic conductivity. In addition, a comprehensive assessment was conducted for 17 cation dopants, examining their influence on the thermodynamic, moisture, and electrochemical stabilities of the LZC system, including the width of the electrochemical window and interfacial compatibility with representative cathode materials as well as with sulfide- and oxide-based SSEs. Among the candidates, Bi doping emerged as particularly promising, as it reduced the E_a barrier along the ab-plane while offering a cost advantage over Zr. The resulting Bi-doped compound, LZBiC, demonstrated an average room-temperature ionic conductivity of 10.93 mS cm $^{-1}$ and an average E_a of 241.77 meV, representing an order-of-magnitude improvement over pure LZC. The experimental results also demonstrate that Bi doping has a significant promoting effect on the enhancement of LZC conductivity. In-depth analysis revealed a shift in the Li-ion transport mechanism from short-range cooperative migration observed in pure LZC to long-range cooperative migration observed in LZBiC. This shift is attributed to the destabilization of the original octahedral-tetrahedral-octahedral framework by Bi doping, which renders Li sites metastable and promotes extended cooperative ion motion. Br-substitution in LZC causes pronounced lattice expansion and increases the polarizability of the anion framework. These changes enlarge the Li-ion migration space and soften the M-X-Li-X-M backbone, thereby lowering the sensitivity to cation disorder and enhancing ionic conductivity. AIMD simulations further confirm that Br doping significantly improves Li-ion mobility while preserving interfacial stability with high-voltage cathode materials.

Finally, we examined the correlation between Li-Li nearestneighbor distances and ionic transport properties across various SSE systems. The results suggest that shorter Li-Li separations tend to correspond to lower activation energies and higher ionic conductivities. Such proximity promotes enhanced electrostatic interaction and facilitates chain-like cooperative migration mechanisms.

This work establishes a long-range cooperative transport mechanism in halide solid-state electrolytes and identifies Bidoped LZBiC as a cost-effective, high-performance candidate while also elucidating the critical structure—property relationships governing Li-ion transport. Future studies should further

investigate Li-ion migration in the amorphous LZC framework, as well as the synergistic effects of codoping with Bi cations and Br anions, to gain a more comprehensive understanding of their influence on ionic transport behavior and structural stability. The findings reported herein provide valuable guidance for the rational design of high-performance halide-based solid-state electrolytes.

ASSOCIATED CONTENT

Supporting Information

The Supporting Information is available free of charge at https://pubs.acs.org/doi/10.1021/acs.chemmater.5c01711.

Details of the computational methods, theoretical analyses, calculation formulas, Li-ion migration pathways, reaction energies, electrochemical stability, ionic transport properties, and interfacial reactions (PDF)

AUTHOR INFORMATION

Corresponding Author

Bingkai Zhang — School of Chemical Engineering and Light Industry, Guangdong University of Technology, Guangzhou 510006, China; orcid.org/0009-0008-1563-3931; Email: zhangbk@gdut.edu.cn

Authors

Ruishan Zhang — School of Chemical Engineering and Light Industry, Guangdong University of Technology, Guangzhou 510006, China

Shunning Li — School of Advanced Materials, Peking University Shenzhen Graduate School, Shenzhen 518055, China; orcid.org/0000-0002-5381-6025

Feng Pan — School of Advanced Materials, Peking University Shenzhen Graduate School, Shenzhen 518055, China; orcid.org/0000-0002-8216-1339

Complete contact information is available at: https://pubs.acs.org/10.1021/acs.chemmater.5c01711

Notes

The authors declare no competing financial interest.

ACKNOWLEDGMENTS

This research work was supported by the Province Natural Science Fund of Guangdong (2024A1515030261) and the Guangdong Key Laboratory of Design and Calculation of New Energy Materials (No. 2017B030301013). We also acknowledge the support from the Shenzhen Key Laboratory of Solid State Batteries (SYSPG20241211173726011). We are grateful to Prof. Songbai Han from the Shenzhen Key Laboratory of Solid State Batteries, Southern University of Science and Technology, Shenzhen 518055, China, and Daotong Yang from the College of Chemistry, Jilin University, Qianjin Street 2699, Changchun 130012, P. R. China, for their valuable support.

■ REFERENCES

- (1) Janek, J.; Zeier, W. G. A Solid Future for Battery Development. *Nat. Energy* **2016**, *1* (9), 16141.
- (2) Wang, D.; Jiao, Y.; Shi, W.; Pu, B.; Ning, F.; Yi, J.; Ren, Y.; Yu, J.; Li, Y.; Wang, H.; Li, B.; Li, Y.; Nan, C.; Chen, L.; Shi, S. Fundamentals and Advances of Ligand Field Theory in Understanding Structure-Electrochemical Property Relationship of Intercalation-Type Electrode Materials for Rechargeable Batteries. *Prog. Mater. Sci.* 2023, 133, 101055.

- (3) Yang, H.; Wu, N. Ionic conductivity and ion transport mechanisms of solid-state lithium-ion battery electrolytes: A review. *Energy Sci. Eng.* **2022**, *10* (5), 1643–1671.
- (4) Gao, X.; Liu, B.; Hu, B.; Ning, Z.; Jolly, D. S.; Zhang, S.; Perera, J.; Bu, J.; Liu, J.; Doerrer, C.; et al. Solid-State Lithium Battery Cathodes Operating at Low Pressures. *Joule* **2022**, *6* (3), 636–646.
- (5) Tanaka, Y.; Ueno, K.; Mizuno, K.; Takeuchi, K.; Asano, T.; Sakai, A. New Oxyhalide Solid Electrolytes with High Lithium Ionic Conductivity > 10 mS cm⁻¹ for All-solid-state Batteries. *Angew. Chem., Int. Ed.* **2023**, 62 (13), No. e202217581.
- (6) Li, X.; Liang, J.; Yang, X.; Adair, K. R.; Wang, C.; Zhao, F.; Sun, X. Progress and Perspectives on Halide Lithium Conductors for All-Solid-State Lithium Batteries. *Energy Environ. Sci.* **2020**, *13* (5), 1429–1461.
- (7) Asano, T.; Sakai, A.; Ouchi, S.; Sakaida, M.; Miyazaki, A.; Hasegawa, S. Solid Halide Electrolytes with High Lithium-ion Conductivity for Application in 4 V Class Bulk-type All-solid-state Batteries. *Adv. Mater.* **2018**, *30* (44), 1803075.
- (8) Nikodimos, Y.; Su, W.-N.; Hwang, B. J. Halide Solid-state Electrolytes: Stability and Application for High Voltage All-solid-state Li Batteries. *Adv. Energy Mater.* **2023**, *13* (3), 2202854.
- (9) Hu, L.; Wang, J.; Wang, K.; Gu, Z.; Xi, Z.; Li, H.; Chen, F.; Wang, Y.; Li, Z.; Ma, C. A cost-effective, ionically conductive and compressible oxychloride solid-state electrolyte for stable all-solid-state lithium-based batteries. *Nat. Commun.* **2023**, *14* (1), 3807.
- (10) Wang, K.; Ren, Q.; Gu, Z.; Duan, C.; Wang, J.; Zhu, F.; Fu, Y.; Hao, J.; Zhu, J.; He, L.; Wang, C.-W.; Lu, Y.; Ma, J.; Ma, C. A cost-effective and humidity-tolerant chloride solid electrolyte for lithium batteries. *Nat. Commun.* **2021**, *12* (1), 4410.
- (11) Kwak, H.; Han, D.; Lyoo, J.; Park, J.; Jung, S. H.; Han, Y.; Kwon, G.; Kim, H.; Hong, S.; Nam, K.; Jung, Y. S. New Cost-Effective Halide Solid Electrolytes for All-Solid-State Batteries: Mechanochemically Prepared Fe³⁺-Substituted Li₂ZrCl₆. Adv. Energy Mater. **2021**, 11 (12), 2003190.
- (12) Yu, J.; Wang, D.; Wang, G.; Cui, Y.; Shi, S. Breaking the Electronic Conductivity Bottleneck of Manganese Oxide Family for High-power Fluorinated Graphite Composite Cathode by Ligand-field High-dimensional Constraining Strategy. *Adv. Mater.* **2023**, 35 (8), 2209210.
- (13) Luo, X.; Zhong, Y.; Wang, X.; Xia, X.; Gu, C.; Tu, J. Ionic Conductivity Enhancement of Li₂ZrCl₆ Halide Electrolytes via Mechanochemical Synthesis for All-Solid-State Lithium—Metal Batteries. ACS Appl. Mater. Interfaces 2022, 14 (44), 49839–49846.
- (14) Gao, K.-N.; Bai, F.; Sun, Z.; Zhang, T. Aliovalent Substitution of Al³⁺ in Li₂ZrCl₆ Solid Electrolyte towards Large-Scale Application. *Energy Storage Mater.* **2024**, *70*, 103444.
- (15) Chen, S.; Yu, C.; Wei, C.; Jiang, Z.; Zhang, Z.; Peng, L.; Cheng, S.; Xie, J. Unraveling Electrochemical Stability and Reversible Redox of Y-Doped Li₂ZrCl₆ Solid Electrolytes. *Energy Mater. Adv.* **2023**, *4*, 2010
- (16) Kwak, H.; Han, D.; Son, J. P.; Kim, J. S.; Park, J.; Nam, K.-W.; Kim, H.; Jung, Y. S. Li $^+$ Conduction in Aliovalent-Substituted Monoclinic Li $_2$ ZrCl $_6$ for All-Solid-State Batteries: Li $_{2+x}$ Zr $_{1-x}$ M $_x$ Cl $_6$ (M = In, Sc). Chem. Eng. J. 2022, 437, 135413.
- (17) Park, K.-H.; Kaup, K.; Assoud, A.; Zhang, Q.; Wu, X.; Nazar, L. F. High-Voltage Superionic Halide Solid Electrolytes for All-Solid-State Li-Ion Batteries. ACS Energy Lett. 2020, 5 (2), 533–539.
- (18) Ganesan, P.; Soans, M.; Cambaz, M. A.; Zimmermanns, R.; Gond, R.; Fuchs, S.; Hu, Y.; Baumgart, S.; Sotoudeh, M.; Stepien, D.; Stein, H.; Groß, A.; Bresser, D.; Varzi, A.; Fichtner, M. Fluorine-Substituted Halide Solid Electrolytes with Enhanced Stability toward the Lithium Metal. ACS Appl. Mater. Interfaces 2023, 15 (32), 38391–38402.
- (19) Kresse, G.; Hafner, J. Ab Initio Molecular-Dynamics Simulation of the Liquid-Metal—Amorphous-Semiconductor Transition in Germanium. *Phys. Rev. B* **1994**, 49 (20), 14251.
- (20) Kresse, G.; Joubert, D. From Ultrasoft Pseudopotentials to the Projector Augmented-Wave Method. *Phys. Rev. B* **1999**, *59* (3), 1758.

- (21) Grimme, S. Semiempirical GGA-type Density Functional Constructed with a Long-range Dispersion Correction. *J. Comput. Chem.* **2006**, 27 (15), 1787–1799.
- (22) Moellmann, J.; Grimme, S. DFT-D3 Study of Some Molecular Crystals. *J. Phys. Chem. C* **2014**, *118* (14), 7615–7621.
- (23) Mattsson, A. E.; Armiento, R.; Schultz, P. A.; Mattsson, T. R. Nonequivalence of the Generalized Gradient Approximations PBE and PW91. Phys. Rev. B:Condens. Matter Mater. Phys. 2006, 73 (19), 195123.
- (24) Cuendet, M. A. The Jarzynski Identity Derived from General Hamiltonian or Non-Hamiltonian Dynamics Reproducing NVT or NPT Ensembles. J. Chem. Phys. 2006, 125 (14), 144109.
- (25) Shi, S.; Gao, J.; Liu, Y.; Zhao, Y.; Wu, Q.; Ju, W.; Ouyang, C.; Xiao, R. Multi-Scale Computation Methods: Their Applications in Lithium-Ion Battery Research and Development. *Chin. Phys. B* **2016**, 25 (1), 018212.
- (26) Kob, W.; Andersen, H. C. Testing Mode-Coupling Theory for a Supercooled Binary Lennard-Jones Mixture I: The van Hove Correlation Function. *Phys. Rev. E* **1995**, *51* (5), 4626.
- (27) Michalet, X. Mean Square Displacement Analysis of Single-Particle Trajectories with Localization Error: Brownian Motion in an Isotropic Medium. *Phys. Rev. E* **2010**, 82 (4), 041914.
- (28) Arffman, A.; Juuti, P.; Harra, J.; Keskinen, J. Differential Diffusion Analyzer. *Aerosol Sci. Technol.* **2017**, *51* (12), 1429–1437.
- (29) Li, X.; Kim, J. T.; Luo, J.; Zhao, C.; Xu, Y.; Mei, T.; Li, R.; Liang, J.; Sun, X. Structural Regulation of Halide Superionic Conductors for All-Solid-State Lithium Batteries. *Nat. Commun.* **2024**, *15* (1), 53.
- (30) Park, J.; Han, D.; Kwak, H.; Han, Y.; Choi, Y. J.; Nam, K.-W.; Jung, Y. S. Heat Treatment Protocol for Modulating Ionic Conductivity via Structural Evolution of $\text{Li}_{3\text{-x}}\text{Yb}_{1\text{-x}}\text{M}_{x}\text{Cl}_{6}$ (M = Hf⁴⁺, Zr⁴⁺) New Halide Superionic Conductors for All-Solid-State Batteries. Chem. Eng. J. **2021**, 425, 130630.
- (31) Luo, X.; Hu, X.; Zhong, Y.; Wang, X.; Tu, J. Degradation Evolution for Li_2ZrCl_6 Electrolytes in Humid Air and Enhanced Air Stability via Effective Indium Substitution. *Small* **2024**, 20 (10), 2306736.
- (32) Jeon, H.-J.; Subramanian, Y.; Ryu, K.-S. Variation of Electrochemical Performance of Li2ZrCl6 Halide Solid Electrolyte with Mn Substitution for All-Solid-State Batteries. *J. Power Sources* **2024**, *602*, 234343.
- (33) Van Der Maas, E.; Famprikis, T.; Pieters, S.; Dijkstra, J. P.; Li, Z.; Parnell, S. R.; Smith, R. I.; Van Eck, E. R. H.; Ganapathy, S.; Wagemaker, M. Re-Investigating the Structure–Property Relationship of the Solid Electrolytes $\text{Li}_{3-x}\text{In}_{1-x}\text{Zr}_x\text{Cl}_6$ and the Impact of In–Zr(iv) Substitution. *J. Mater. Chem. A* **2023**, *11* (9), 4559–4571.
- (34) Helm, B.; Schlem, R.; Wankmiller, B.; Banik, A.; Gautam, A.; Ruhl, J.; Li, C.; Hansen, M. R.; Zeier, W. G. Exploring Aliovalent Substitutions in the Lithium Halide Superionic Conductor $\text{Li}_{3-x}\text{In}_{1-x}\text{Zr}_x\text{Cl}_6$ (0 $\leq x \leq$ 0.5). *Chem. Mater.* **2021**, 33 (12), 4773–4782.
- (35) Kim, S. Y.; Kaup, K.; Park, K.-H.; Assoud, A.; Zhou, L.; Liu, J.; Wu, X.; Nazar, L. F. Lithium Ytterbium-Based Halide Solid Electrolytes for High Voltage All-Solid-State Batteries. *ACS Materials Lett.* **2021**, 3 (7), 930–938.
- (36) Schlem, R.; Muy, S.; Prinz, N.; Banik, A.; Shao-Horn, Y.; Zobel, M.; Zeier, W. G. Mechanochemical Synthesis: A Tool to Tune Cation Site Disorder and Ionic Transport Properties of Li₃MCl₆ (M = Y, Er) Superionic Conductors. *Adv. Energy Mater.* **2020**, *10* (6), 1903719.
- (37) Wang, L.; Xiao, W.; Sun, L.; Yang, R.; Yu, J.; Wang, L. Atomistic Mechanism of High Ionic Conductivity in Lithium Ytterbium-Based Halide Solid Electrolytes: A First-Principles Study. *J. Rare Earths* **2024**, *42* (1), 155–162.
- (38) Yu, T.; Wang, L.; Sun, Q.; Xiao, B.; Bai, X.; Yang, R.; Duan, Y.; Wu, Y.; Li, G.; Xu, G.; Zhao, S.; Wang, L.; Yu, J.; Wang, J. Enabling High Ionic Conductivity in Yttrium-Based Lithium Halide Electrolytes by Composition Modulation for All-Solid-State Batteries. *Mater. Today Chem.* **2023**, *30*, 101510.

- (39) Okhotnikov, K.; Charpentier, T.; Cadars, S. Supercell Program: A Combinatorial Structure-Generation Approach for the Local-Level Modeling of Atomic Substitutions and Partial Occupancies in Crystals. *J. Cheminf.* **2016**, *8*, 17.
- (40) He, B.; Chi, S.; Ye, A.; Mi, P.; Zhang, L.; Pu, B.; Zou, Z.; Ran, Y.; Zhao, Q.; Wang, D.; Zhang, W.; Zhao, J.; Adams, S.; Avdeev, M.; Shi, S. High-throughput screening platform for solid electrolytes combining hierarchical ion-transport prediction algorithms. *Data* **2020**, *7* (1), 151.
- (41) Zhang, L.; He, B.; Zhao, Q.; Zou, Z.; Chi, S.; Mi, P.; Ye, A.; Li, Y.; Wang, D.; Avdeev, M.; Adams, S.; Shi, S. A Database of Ionic Transport Characteristics for over 29000 Inorganic Compounds. *Adv. Funct. Mater.* **2020**, *30* (35), 2003087.
- (42) Shi, J.; Yao, Z.; Xiang, J.; Cai, C.; Tu, F.; Zhang, Y.; Yao, W.; Jia, Q.; Zhou, Y.; Shen, S.; Yang, Y. High-Conductivity Li₂ZrCl₆ Electrolytes via an Optimized Two-Step Ball-Milling Method for All-Solid-State Lithium—Metal Batteries. *ACS Sustainable Chem. Eng.* **2024**, *12*, 2009–2017.
- (43) Zhang, H.; Yu, Z.; Chen, H.; Zhou, Y.; Huang, X.; Tian, B. Li-Richening Strategy in Li₂ZrCl₆ Lattice towards Enhanced Ionic Conductivity. *J. Energy Chem.* **2023**, *79*, 348–356.
- (44) He, X.; Zhu, Y.; Mo, Y. Origin of Fast Ion Diffusion in Super-Ionic Conductors. *Nat. Commun.* **2017**, 8 (1), 15893.
- (45) Shadike, Z.; Zhou, Y.-N.; Chen, L.-L.; Wu, Q.; Yue, J.-L.; Zhang, N.; Yang, X.-Q.; Gu, L.; Liu, X.-S.; Shi, S.-Q.; Fu, Z.-W. Antisite occupation induced single anionic redox chemistry and structural stabilization of layered sodium chromium sulfide. *Nat. Commun.* **2017**, *8* (1), 566.
- (46) Li, Z.; Dong, H.; Zhang, B. Motif-Based Exploration of Halide Classes of $\text{Li}_5\text{M1}_{0.5}\text{M2}_{0.5}\text{X}_8$ Conductors Using the DFT Method: Toward High Li-Ion Conductivity and Improved Stability. *ACS Appl. Mater. Interfaces* **2023**, *15* (36), 42481–42489.
- (47) Wang, Z.; Ha, J.; Kim, Y. H.; Im, W. B.; McKittrick, J.; Ong, S. P. Mining Unexplored Chemistries for Phosphors for High-Color-Quality White-Light-Emitting Diodes. *Joule* **2018**, 2 (5), 914–926.
- (48) Li, X.; Liang, J.; Chen, N.; Luo, J.; Adair, K. R.; Wang, C.; Banis, M. N.; Sham, T.; Zhang, L.; Zhao, S.; Lu, S.; Huang, H.; Li, R.; Sun, X. Water-mediated Synthesis of a Superionic Halide Solid Electrolyte. *Angew. Chem., Int. Ed.* **2019**, 58 (46), 16427–16432.
- (49) Li, X.; Liang, J.; Luo, J.; Norouzi Banis, M.; Wang, C.; Li, W.; Deng, S.; Yu, C.; Zhao, F.; Hu, Y.; et al. Air-Stable Li_3InCl_6 Electrolyte with High Voltage Compatibility for All-Solid-State Batteries. *Energy Environ. Sci.* **2019**, 12 (9), 2665–2671.
- (50) Shou, Y.; Ou, J.; Li, C.; Huang, J.; Zhao, T.; Fang, Y.; Kang, Y.; Zhao, Y.; Huang, M.; Zhao, C. Achieving Highly Reversible All-Solid-State Lithium-Sulfur Batteries through Metal—Sulfur Bonding Regulation. ACS Mater. Lett. 2024, 6 (10), 4545—4554.
- (51) Zhu, Y.; He, X.; Mo, Y. Origin of Outstanding Stability in the Lithium Solid Electrolyte Materials: Insights from Thermodynamic Analyses Based on First-Principles Calculations. ACS Appl. Mater. Interfaces 2015, 7 (42), 23685–23693.
- (52) Zhang, B.; Zhong, J.; Pan, F.; Lin, Z. Potential Solid-State Electrolytes with Good Balance between Ionic Conductivity and Electrochemical Stability: Li5– xM1– xMx′O4(M = Al and Ga and M′ = Si and Ge). ACS Appl. Mater. Interfaces 2021, 13 (51), 61296–61304.
- (53) Zhang, B.; Lin, Z.; Dong, H.; Wang, L.-W.; Pan, F. Revealing Cooperative Li-Ion Migration in $\text{Li}_{1+x}\text{Al}_x\text{Ti}_{2-x}(\text{PO}_4)_3$ Solid State Electrolytes with High Al Doping. *J. Mater. Chem. A* **2020**, 8 (1), 342–348.
- (54) Zhang, B.; Weng, M.; Lin, Z.; Feng, Y.; Yang, L.; Wang, L.; Pan, F. Li-ion Cooperative Migration and Oxy-sulfide Synergistic Effect in $\mathrm{Li}_{14}P_2\mathrm{Ge}_2\mathrm{S}_{16-6x}\mathrm{O}_x$ Solid-state-electrolyte Enables Extraordinary Conductivity and High Stability. *Small* **2020**, *16* (11), 1906374.
- (55) Zou, Z.; Ma, N.; Wang, A.; Ran, Y.; Song, T.; Jiao, Y.; Liu, J.; Zhou, H.; Shi, W.; He, B.; Wang, D.; Li, Y.; Avdeev, M.; Shi, S. Relationships between Na⁺ Distribution, Concerted Migration, and Diffusion Properties in Rhombohedral NASICON. *Adv. Energy Mater.* **2020**, *10* (30), 2001486.

(56) Zhang, B.; Yang, L.; Wang, L.-W.; Pan, F. Cooperative Transport Enabling Fast Li-Ion Diffusion in Thio-LISICON $\operatorname{Li}_{10}\operatorname{SiP}_2S_{12}$ Solid Electrolyte. *Nano Energy* **2019**, *62*, 844–852. (57) Zhang, B.; Yang, L.; Wang, L.-W.; Pan, F. Cooperative Transport Enabling Fast Li-Ion Diffusion in Thio-LISICON $\operatorname{Li}_{10}\operatorname{SiP}_2S_{12}$ Solid Electrolyte. *Nano Energy* **2019**, *62*, 844–852.

